Beacon satellite receiver for ionospheric tomography

J. Vierinen,[1] J. Norberg,[2] M. S. Lehtinen,[3] O. Amm,[2] L. Roininen,[3] A.

Väänänen,[3] P. J. Erickson[1] D. McKay-Bukowski,[3]

[1]Haystack Observatory, Massachusetts

Institute of Technology, Westford,

Massachusetts, USA.

[2]Finnish Meteorological Institute,

Helsinki, Finland.

[3]Sodankylä Geophysical Observatory,

University of Oulu, Sodankylä, Finland.

We introduce a new coherent dual channel beacon satellite receiver intended for ionospheric tomography. The measurement equation includes neutral atmosphere and ionosphere propagation effects, relative errors in satellite and receiver clocks, and residual Doppler shifts caused by errors in the satellite ephemeris. We also investigate the distribution of errors for phase curve measurements and the use of phase curve measurements for limited angle tomography using the framework of statistical linear inverse problems. We describe the design of our beacon satellite receiver software, and present one possible hardware configuration. Finally, we present results obtained using a network of four newly developed receivers and compare the results with those of an existing ionospheric tomography network at Sodankylä Geophysical Observatory.

1. Introduction

Ground based ionospheric tomography is a method for estimating ionospheric electron density using measurements of ionospheric delay as electromagnetic waves transmitted from satellites are received at multiple ground stations [*Austen et al.*, 1988; *Raymund et al.*, 1990; *Kunitsyn et al.*, 1994; *Markkanen et al.*, 1995; *Nygrén et al.*, 1996; *Mitchell et al.*, 1997; *Bernhardt et al.*, 1998; *Kunitsyn and Tereshchenko*, 2003; *Garner et al.*, 2009]. There are two main families of satellites that can be used for this purpose: low Earth orbit beacons, and global navigation satellites. We will focus in this work on low earth orbit (LEO) satellites that transmit phase coherent 150/400 MHz signals. These are of interest especially for local high resolution tomography, as lower frequencies are more affected by the ionosphere than global navigation satellite frequencies. LEO satellites also have fast ground station transit times, providing significantly greater independent measurements of line integrals within a given time interval. These measurement qualities provide enhanced time resolution of derived ionospheric density structures over that possible with e.g. GPS satellite networks [*Rideout and Coster*, 2006]. Bernhardt and Siefring [2006] provide an overview of coherent beacon satellite theory and operation.

The Sodankylä Geophysical Observatory (SGO) in Finland operates an existing tomography receiver network with receivers that were custom built by Invers Ltd. These receivers rely on a Russian Tsykada navigation satellite system [*Kunitsyn et al.*, 1994] limited to three currently operational transmitting platforms. In order to upgrade these receivers for modern observations, we require a new receiver that

can function autonomously, observe multiple satellites simultaneously, and support all currently operational 150/400 MHz beacon satellites.

One practical way of implementing an ionospheric tomography receiver is using a software defined radio [*Mitola* , 2000; *Reed* , 2002], in which most of the signal processing is performed with software on a general purpose computer. The main advantage of this approach is that the receiver software can be continuously improved, even after deployment of the instrument. Scientific numerical algorithms can also be used, instead of fixed purpose signal processing hardware. An implementation of an open-source software-defined beacon satellite receiver is described by Yamamoto [2008]. In this paper, we will introduce a new beacon receiver that builds on the work of Yamamoto, and is specifically intended for autonomous operation of receivers in a large network configuration.

In the following sections, we derive equations of radio propagation through the atmosphere and describe the fundamentals of a beacon satellite measurement. We then outline the basic principle of tomographic reconstruction of ionospheric electron density using relative propagation time differences measured using a ground based receiver network. After a description of the technical details of our hardware and software, we conclude by presenting results from several newly deployed ionospheric tomography receivers. These results will be compared with data from the existing ionospheric tomography receiver chain operated by the SGO.

2. Atmospheric propagation

The phase velocity of radio waves in a medium is defined as

$$v_p = cn^{-1},$$ (1)

where n is the refractive index of the medium. In the ionosphere, the refractive index of the medium is given by the Appleton-Lassen magnetoionic propagation equation [*Appleton and Chapman*, 1932; *Lassen*, 1927; *Hartree*, 1929]. With the frequencies used in VHF and UHF beacon satellites, it is possible to ignore electron-neutral collisions and the magnetic field. In this case, the refractive index provided by the Appleton-Lassen equation can be approximated using

$$n = \left(1 - \omega_p^2/\omega^2\right)^{\frac{1}{2}},$$ (2)

where $\omega_p = \sqrt{\frac{N_e e^2}{\epsilon_0 m_e}}$ is the electron plasma frequency (rad/s), and ω is the frequency of the radio wave (rad/s). The term N_e is electron density (m^{-3}), e is charge of an electron, ϵ_0 is the permittivity of free space, and m_e is the mass of an electron.

Below 50 km, the refractive index of plasma approaches one as the number density of electrons approaches zero. However, the refractive index of the neutral atmosphere starts becoming significant as the density of air grows. The lower atmospheric refractive index n_{tr} of radio waves below 20 GHz is assumed to be non-dispersive, and can be related to the pressure, temperature and humidity of air using the following formula [*Rüeger*, 2002]

$$\begin{aligned} n_{\mathrm{tr}} = 1 + 10^{-6}\Bigg(&77.68\frac{p_d}{T} + 71.30\frac{p_w}{T} + \\ &3.75 \cdot 10^{-5}\frac{p_w}{T^2}\Bigg), \end{aligned}$$ (3)

where p_d is the partial pressure of dry air (hPa), T is the temperature (K), p_w is the

partial pressure of water vapor (hPa). We will not discuss inversion of tropospheric

water vapor parameters [*Bernhardt et al.* , 2000] in this work, but we will investigate

the effect of the tropospheric propagation for the relative phase curve measurement.

For this, it is sufficient that we represent the refractive index in the simple form

$$n_{\mathrm{tr}} = 1 + \Delta n_{\mathrm{tr}}, \tag{4}$$

where the small perturbation in the refractive index Δn_{tr} is equivalent to the second

term on the right-hand side of Eq. (3).

We assume that an electromagnetic wave propagates from the satellite to a ground

station along the axis z, with distance L between the satellite and ground station.

In this case, with the satellite at $z = 0$ and phase velocity $v_p(z)$, the electric field

amplitude can be expressed as

$$E(L, t) = E_0 \cos \left(\omega \left(t - \int_0^L dz/v_p(z) \right) \right). \tag{5}$$

From this we can determine the phase $E(L, t) = \cos(\phi'(t))$ of a signal at a ground

station at a time-dependent distance $L(t)$ from the satellite as

$$\phi'(t) = \omega t - \frac{\omega}{c} \int_0^{L(t)} n(z) dz. \tag{6}$$

However, a radio receiver is typically tuned to the center frequency ω, which cancels

out the term ωt and leaves

$$\phi(t) = \phi'(t) - \omega t = -\frac{\omega}{c} \int_0^{L(t)} n(z) dz. \tag{7}$$

In order to convert this into an integral of $N_e(z)$, we use the approximative form of

the refractive index in Eq. (2) to determine the electron density as a function of the

refractive index

$$N_e(z) = -\frac{\epsilon_0 m_e \omega^2}{e^2}(n(z)^2 - 1). \tag{8}$$

By approximating this as a first order Taylor polynomial expanded around $n(z) = 1$ we obtain

$$N_e(z) \approx -\frac{2\epsilon_0 m_e \omega^2}{e^2}(n(z) - 1), \tag{9}$$

which is a good approximation when $\omega \gg \omega_p$ [$Davies$, 1965]. Using this, we get a formula for $n(z)$:

$$n(z) \approx 1 - \frac{e^2}{2\epsilon_0 m_e \omega^2}N_e(z). \tag{10}$$

If we now combine Eqs. (10) and (4) and insert them into Eq. (7), we get

$$\phi(t) = -\frac{\omega}{c}L(t) + \frac{a}{\omega}\int_{L_0(t)}^{L(t)} N_e(z)dz - \\ \frac{\omega}{c}\int_0^{L_0(t)} \Delta n_{\text{tr}}(z)dz, \tag{11}$$

where $a = \frac{e^2}{2\epsilon_0 m_e c}$. The above equation relates the measured phase to the line integral of electron density and the line integral of the perturbations in the refractive index caused by lower atmospheric propagation. Here the term $L(t)$ contributes to the Doppler shift of the signal in vacuum. This is typically known to some accuracy, and it can also be removed by adjusting the center frequency of the receiver correspondingly. However, we will leave this term in order to show how errors in $L(t)$ will affect the signal. The range $L_0(t)$ corresponds to the range where the refractive index transitions from tropospheric refractive index to ionospheric refractive index. We can make this assumption, as there is no appreciable overlap between those altitudes where ionospheric refractive index and the neutral atmosphere refractive index is significantly different from 1.

When receiving a signal for the first time after the satellite rises above the horizon, practical measurements of $\phi(t)$ have the difficulty of unknown initial phase γ due to the inherent 2π phase ambiguity. Additional errors are also introduced by unknown relative clock drifts of the satellite and the ground station, as well as uncertainties in the distance between the satellite and the ground station, which are all here denoted by a random variable $r(t)$. In practice, our measured phase curve will be of the form

$$
\begin{aligned}
\phi(t) =& \gamma - \frac{\omega}{c}(L(t) + r(t)) + \\
& \frac{a}{\omega} \int_{L_0(t)}^{L(t)} N_e(z)dz - \frac{\omega}{c} \int_0^{L_0(t)} \Delta n_{\mathrm{tr}}(z)dz.
\end{aligned}
\tag{12}
$$

Using $L(t)$ for the upper bound of the integral is a sufficiently good approximation as the errors in range are insignificant $r(t) \ll L(t)$. We can also write this in more concise form as follows:

$$
\phi(t) = \gamma + \omega\zeta(t) + \frac{a}{\omega} \int_{L_0(t)}^{L(t)} N_e(z)dz,
\tag{13}
$$

where

$$
\zeta(t) = -\frac{1}{c} \left(L(t) + r(t) + \int_0^{L_0(t)} \Delta n_{\mathrm{tr}}(z)dz \right).
\tag{14}
$$

When estimating total electron content using dual frequency beacon satellites, two simultaneous measurements of $\phi(t)$ are made at two different frequencies, i.e.,

$$
\begin{aligned}
\phi_1(t) =& \gamma_1 + a\omega_1^{-1} \int_{L_0(t)}^{L(t)} N_e(z)dz + \zeta(t)\omega_1 \\
\phi_2(t) =& \gamma_2 + a\omega_2^{-1} \int_{L_0(t)}^{L(t)} N_e(z)dz + \zeta(t)\omega_2
\end{aligned}
\tag{15}
$$

When we multiply $\phi_1(t)$ with $\frac{\omega_2}{\omega_1}$ and subtract $\phi_2(t)$ from it, the term $\zeta(t)$ is cancelled out up to an unknown constant $\gamma' = \frac{\omega_2}{\omega_1}\gamma_1 - \gamma_2$ and we obtain

$$
\frac{\omega_2}{\omega_1}\phi_1(t) - \phi_2(t) = \gamma' + a \left(\frac{\omega_2}{\omega_1^2} - \frac{1}{\omega_2} \right) \int_{L_0(t)}^{L(t)} N_e(z)dz,
$$

where the contribution of $\zeta(t)$ is completely eliminated. This also has the benefit of eliminating lower atmospheric propagation effects, relative clock errors, and trajectory errors. We can express this in another way as

$$
\begin{aligned}
\Delta\phi_{12}(t) =& \gamma'' + \int_{L_0(t)}^{L(t)} N_e(z)dz \\
=& \frac{1}{a}\left(\frac{\omega_2}{\omega_1^2} - \frac{1}{\omega_2}\right)^{-1}\left(\frac{\omega_2}{\omega_1}\phi_1(t) - \phi_2(t)\right),
\end{aligned}
\tag{16}
$$

where $\Delta\phi_{12}(t)$ is the so called relative total electron content, comprising the line integral of electron density along the path between the satellite and the receiver, up to an unknown constant γ''. This is the basic measurement that goes into the ionospheric tomography inversion procedure, which determines γ'' and $N_e(z)$ from simultaneous observations at multiple stations.

In practice, relative total electron content is typically measured at 1-50 Hz sampling rate during the pass of a satellite. We assume that $\Delta\phi_{12}(t)$ changes slowly as a function of time, which allows us to unwrap 2π phase ambiguities by selecting the smallest of the possible phase differences. However, if one of the satellite signals is lost for a sufficiently long time, removing this phase ambiguity becomes more difficult. In this case, one sensible option is to split the phase curves into two phase curves with independent unknown constants.

Using a similar well-known subtraction procedure [*Danchik* , 1998], we can also estimate $\zeta(t)$, which contains information about the troposphere, the clock errors, and the satellite trajectory errors. In this case, we multiply $\phi_1(t)$ with ω_1 and $\phi_2(t)$

with ω_2 and then we subtract the first from the second to obtain

$$\zeta(t) = \gamma + \frac{\omega_1 \phi_1(t) - \omega_2 \phi_2(t)}{\omega_1^2 - \omega_2^2}, \tag{17}$$

where γ is again an unknown constant. This measurement has the considerable benefit of eliminating ionospheric effects. If the trajectory is known to a good enough accuracy ($r(t)$ is small), then it is possible to make inferences of the tropospheric refractive index. The measurement $\zeta(t)$ can be also be used to perform accurate orbital elements using multiple receiver stations [*Izsak*, 1960].

3. Measurement errors

Correct modeling of errors in phase curve measurements is important for ionospheric tomography. To correctly express phase errors, we first inspect a discretized baseband measurement of a signal $s_t = ae^{i\phi_t} \in \mathbb{C}$, contaminated with noise that affects the amplitude and phase of the signal. This is in essence the measurement $m_t \in \mathbb{C}$ of a beacon satellite transmission

$$m_t = s_t + \xi_t = (a + \xi^a)e^{i(\theta_t + \xi_t^\theta)}. \tag{18}$$

Here ξ^a and ξ_t^θ are real-valued random processes that describe the amplitude and phase noise of the measurement. When assuming small enough additive Gaussian noise $\xi_t \sim N_{\mathbb{C}}(0, \sigma^2)$, ξ^a and ξ_t^θ can also be approximated as Gaussian noise.

When estimating the differential phase curve $\phi_t \in \mathbb{R}$, we examine the phase increment associated with each measurement m_t and cumulatively sum this together

$$\phi_t = \sum_{n=0}^{t} \text{Arg}(m_n/m_{n-1}), \tag{19}$$

or

$$\phi_t = \sum_{n=0}^{t} \theta_n - \theta_{n-1} + \xi_n^\theta - \xi_{n-1}^\theta. \tag{20}$$

Assuming that $\theta_n - \theta_{n-1} + \xi_n^\theta - \xi_{n-1}^\theta \ll 2\pi$, the cumulative summation does not lead to a cumulative error. To see this, we first investigate what happens at the initial step, $t = 1$

$$\phi_1 = \theta_1 - \theta_0 + \xi_1^\theta - \xi_0^\theta. \tag{21}$$

At $t = 2$, we get

$$\phi_2 = \sum_{n=0}^{2} (\theta_n - \theta_{n-1}) + \xi_2^\theta - \xi_0^\theta, \tag{22}$$

as ξ_1^θ cancels out. Through induction, we can then see that on step $t + 1$, we only have two noise terms, composed of initial error ξ_0^θ and a new term ξ_{t+1}^θ. All of the intermediate noise terms have cancelled out in the successive cumulative sums.

$$\phi_{t+1} = \sum_{n=0}^{t+1} (\theta_n - \theta_{n-1}) + \xi_{t+1}^\theta - \xi_0^\theta. \tag{23}$$

Thus, for small enough errors, we can assume that the phase curve error is an identically distributed and independent Gaussian random variable. However, if the random errors are too large, there will be a 2π ambiguity that cannot be removed.

Simulated phase curve errors for several different signal to noise ratios are depicted in Figure 1. These were done by using equation 18 with constant signal $s_t = 1$, and added complex Gaussian random noise with variance $\sigma_t \sim N_\mathbb{C}(0, \mathrm{SNR}^{-1})$. In this simulation, it is apparent that with a SNR of 10 dB, the errors are zero mean and they are not cumulative. With a SNR of 3 dB, the additive noise occasionally causes

a 2π jump in either direcion. In the case of a SNR of -10 dB, the signal resembles a random walk with uniformly distributed $[-\pi, \pi]$ steps in phase.

In order to properly handle cases where there is a significant drift of phase due to poor SNR, one possibility is to examine the SNR and to simple determine that the phase curve is not continuous anymore at the location where large erroneous drifts in phase are expected. In this case, when performing tomographic inversion, there will be multiple independent phase curves during each satellite overpass. This is discussed in section 4.

In practice, there are also other signal degrading factors that cause errors when estimating the phase curve. Signals from other beacon satellites, and other man made radio noise can cause large erroneous drifts in the phase curve. In practice, these cannot be detected from SNR alone. In this case, one option is to search for large sudden jumps in the phase curve.

4. Tomographic reconstruction

The purpose of a tomographic reconstruction of the ionosphere is to estimate the two- or three-dimensional electron density function $N_e(\mathbf{p})$ from phase curves measured during a satellite pass on multiple receiver stations. Here $\mathbf{p}$ represents a spatial coordinate. A conceptual diagram of a beacon satellite measurement is shown in Figure 2.

This problem, which is sometimes called the limited angle tomography problem [*Kaipio and Somersalo* , 2005], is ill-posed in the sense that the measurements do not

contain enough information so that a unique solution for the unknown can be found. In order to get an estimate for the unknown, some additional information is therefore needed to stabilize the problem. In the case of ionospheric tomography, multiple possible approaches exist. One common method is to assume that the solution is spatially smooth and temporally unchanged during the time when the satellite passes over the receivers.

Numerically, the problem is solved by parametrizing $N_e(\mathbf{p})$ in some way, i.e., using the form $N_e(\mathbf{p}; \boldsymbol{\theta})$ where $\boldsymbol{\theta} \in \mathbb{R}^{N_p}$ denotes the finite set of model parameters that define the electron density within the volume, and N_p is the number of parameters.

In order to relate the measurements to the unknown parameters, the line integrals in equation (16) must be approximated in some way. The most straightforward way to do this is to utilize the Riemann sum approximation for a line integral through the parameterized medium. We also have to take into account the fact that each phase curve measurement $m_{t,n}$ has an unknown constant phase offset γ_n, and is contaminated with additive noise $\xi_{t,n}$. Each station producing an independent phase curve is indexed here with n. Thus, our measurement equation for each observation becomes

$$m_{t,n} = \frac{1}{N} \sum_{i=1}^{N} N_e(\mathbf{l}_i^{t,n}; \boldsymbol{\theta}) + \gamma_n + \xi_{t,n}, \qquad (24)$$

where $\mathbf{l}_i^{t,n}$ denotes the location of the ith point along the Riemann sum with N partitions, and t denotes a time point on the measured phase curve.

If the relation between the model parameters and the unknown is linear, then the Riemann sum can be written in the following form, where $f(\mathbf{p}) \in \mathbb{R}^{N_p}$ is a vector

valued weighting function that evaluates $N_e(\mathbf{p}; \boldsymbol{\theta})$ at the given point $\mathbf{p}$ according to the interpolation and integration rules. This allows the measurement equation to be written as

$$m_{t,n} = \frac{1}{N} \sum_{i=1}^{N} f(\mathbf{l}_i^{t,n}) \cdot \boldsymbol{\theta} + \gamma_n + \xi_{t,n}, \tag{25}$$

where $\cdot$ denotes a dot product between $f(\boldsymbol{p})$ and $\boldsymbol{\theta}$.

An equation of linear form can be expressed as a linear matrix equation

$$\mathbf{m} = \mathbf{A}\mathbf{x} + \xi, \tag{26}$$

where $\mathbf{m}$ is a vector containing all the phase curve measurements $m_{n,t}$. The vector $\mathbf{x}$ contains the unknown parameters $\boldsymbol{\theta}$ as well as the unknown constant offsets γ_n. The theory matrix $\mathbf{A}$ contains elements that make equations (25) and (26) mathematically equivalent. The vector ξ contains the measurement errors, which are assumed to be normally distributed.

Such a linear problem can be solved within the framework of statistical inverse problems [*Kaipio and Somersalo*, 2005; *Calvetti and Somersalo*, 2007]. The maximum a posteriori estimator for the unknown parameters $\mathbf{x}$ can be written as

$$\hat{\mathbf{x}}_{\mathrm{MAP}} = \boldsymbol{\Sigma}_{\mathrm{post}} \mathbf{A}^{\mathrm{T}} \boldsymbol{\Sigma}^{-1} \mathbf{m}, \tag{27}$$

where

$$\boldsymbol{\Sigma}_{\mathrm{post}} = (\boldsymbol{\Sigma}_{\mathrm{pr}}^{-1} + \mathbf{A}^{\mathrm{T}} \boldsymbol{\Sigma}^{-1} \mathbf{A})^{-1}. \tag{28}$$

In this case, the prior covariance assumption $\boldsymbol{\Sigma}_{\mathrm{pr}}$ is used to stabilize the problem by enforcing smoothness to the solution. This approach is also used by the ionospheric

tomography chain operated by the SGO [*Markkanen et al.* , 1995], and has also been studied e.g. by *Nygrén et al.* [1997].

5. Architecture

Our beacon satellite receiver design can be divided into the following parts:

1. Analog radio front end

2. Coherent dual channel digital receiver

3. General purpose personal computer

4. Software for extracting phase curves from dual-channel digital baseband signals.

The main task of the analog front end is to provide amplified signals from the antenna to the digital receiver. The digital receiver then takes analog signals on two channels (150 and 400 MHz) and produces coherently downconverted digitized baseband signals with sufficient bandwidth to include all beacon satellites of interest. This signal is then transferred to the computer.

This approach has several advantages compared to integrated hardware-based solutions. The software is easily customizable and allows more advanced signal processing methods to be used. The overall cost for developing a software-based system also turns out to be cheaper than developing an integrated hardware-based receiver, as pointed out by [2008].

We have implemented a new receiver based on these underlying principles. All of these programs associated with the receiver can be run in real-time on a standard Linux PC with modest processing capacity. This collection of

programs has been released under the GPL license as a project named Jitter (GNU Ionospheric Tomography Receiver). The software can be downloaded from `http://www.sgo.fi/~j/jitter/web`. This software package will autonomously produce phase curves from satellite passes. (Subsequent tomographic inversion analysis as described in this paper is scheduled for a future software release.)

It should be noted that Prof. Mamoru Yamamoto has also described a relative TEC estimation hardware and software system [*Yamamoto* , 2008] with many similarities to our system. The main difference is that Jitter is designed for autonomous operation in a large network of receivers, and is also capable of simultaneously receiving multiple satellites.

6. Hardware

We have recently deployed six 150/400 MHz beacon satellite receivers as part of Finnish Meteorological Institute's TomoScand project to develop a new 3D ionospheric tomography capability. Four of these receivers are used in the tomography example in this paper. Two more receivers have since been installed (KEV and LYR), but are not used in the results presented in this paper. The locations of all receivers are listed in Table 1. We plan to expand the receiver network in the near future.

The hardware for these receivers consists of a dual band QFH antenna by Nagara Denshi Ltd, a dual band pre-amplifier for the antenna, and an RF front-end stage that is located near the computers. The 150 and 400 MHz channels are received with a single USRP N2x0 series digital receiver equipped with a dual channel TVRX2

daughterboard (50-860 MHz). A block diagram of the receiver hardware is described in Figure 3.

As the data recording portion of the software is written using the Gnuradio open software framework, it is also possible to use other digital receivers with at least two coherent receiver channels, such as the USRP1, USRP E100, or USRP2. The software also supports alternate daughterboard configurations, e.g. WBX or BasicRX daughterboards for receiving the signals. While we discuss dual-band 150/400 MHz satellite observations in this paper, the software itself is general enough that it can be configured to record other frequency pairs as well such as 150/1066 MHz, provided a suitable antenna, RF front end, and digital receiver is used.

7. Software

The software is divided into different subsystems run as separate processes. One process records narrow-band signals to disk on a scheduled basis whenever a satellite is passing a station. Scheduling information including predicted pass times is provided by another process using standard satellite ephemerides routines. A third process is used to analyze the narrow-band recordings, with the help of ephemeris-predicted Doppler shift information to further narrow the bandwidth of the individual channels and to calculate a relative phase difference curve. All of the software written for this package was designed with autonomous long-term operation in mind.

Each day, Jitter automatically retrieves new two-line element (TLE) orbital ephemeris files over the internet from publically available sources (e.g. CelesTrak)

and calculates satellite overflights for the next 24 hours for the configured satellites. This information is written in a compact schedule file that is read by the data recording process. The ephemeris file retrieval and satellite overflight prediction programs are written in Python. The prediction program uses the PyEphem ephemeris package for calculating satellite positions.

The data recording process continuously receives wide-band (typically 1 MHz) signals around the requested frequencies (typically 150 and 400 MHz). This allows the receiver to simultaneously record narrow band signals from multiple satellites transmitting different center frequencies, as long as their center frequency and Doppler shift fits within the wide receiver band. The data recorder process digitally tunes to the center frequency of each satellite when a predicted satellite pass occurs. The signal is digitally band-pass filtered and decimated and the signal from an individual pass is stored on local media in complex single-precision floating point with a sample rate of 40 kHz, which is still large enough to accommodate the Doppler shift of an individual satellite pass. The data recording program is written in C++ using the Gnuradio framework.

The phase curve analysis process reads in newly recorded data files for a satellite pass. It then estimates the Doppler shift of the signal based on the ephemeris file (i.e., $L(t)$) for the satellite. This information is then used to remove the bulk of the Doppler shift of the satellite signal. After this, the remaining Doppler shift is estimated from the data and corrected. This is done by least-squares fitting an outlier-removed seventh-order polynomial to the peak of the dynamic spectrum of

the satellite signal. These operations are performed in an identical (albeit frequency scaled) way for both receiver channels to maintain their phase coherence. Finally, the data is band-pass filtered and decimated with a very narrow band filter (typically 50 Hz) and the differential phase curve $\Delta\phi_t$ is formed by subtracting the frequency scaled phase of one channel from the other $\Delta\phi_t = \frac{3}{8}\phi_t^{400} - \phi_t^{150}$ (last term of Eq. (16)). The resulting relative phase curve and satellite trajectory is stored in a data-file with appropriate metadata (e.g. satellite ID, timestamp, and receiver location). The phase curve analysis program and plotting routines are written in Python, and the data is stored in HDF5 [*Folk et al.* , 2011] format.

8. Satellites

A number of beacon satellites currently exist on orbit with transmissions that can be received with the designed system, but not all of these transmit above a given receiver location for various reasons (e.g. incompatible orbital inclination). In Scandinavia, we have successfully received signals from COSMOS 2407, COSMOS 2414, COSMOS 2429, COSMOS 2463, COSMOS 2454, RADCAL, and DMSP F15. With one receiver located in Ethiopia, we have also recorded the beacon on the C/NOFS satellite. We have also recently received the CERTO beacon on the newly launched ePOP satellite [*Bernhardt and Siefring* , 2006].

9. Example measurement

We perform an example study with COSMOS 2463 satellite overflight measure-ments collected from Scandinavia on 2013-10-23 at 09:50 UTC and produce a tomo-

graphic reconstruction of ionospheric electron density from the collected data. We
chose this particular case due to the projection of the overflight passes between the
receivers, as can be seen in Figure 4.

Data was collected with beacon satellite receivers designed as described in this
paper and installed between 2011 and 2013 by the Finnish Meteorological Institute
on the following four stations: TRO, SOD, MEK, and TAR (Table 1). The locations
are also shown with colored squares on the map in Figure 4.

The satellite overflight takes approximately 15 minutes and we assume a temporally
stationary ionosphere for that duration. In two-dimensional tomography, we also
assume a longitudinally uniform ionosphere in the observation domain.

The software employed for two-dimensional tomography in this example is de-
scribed in the companion paper by Norberg [2014]. The software has been developed
as part of FMI's TomoScand project with the goal of three-dimensional ionospheric
tomography using different data sources, e.g. beacon, GPS satellite, and ionosonde
measurements.

In addition to showing results from new receivers, we compare the results obtained
from the same satellite overflight with an existing receiver chain of four receivers
operated by SGO, shown in Figure 4 with triangles.

9.1. Measurements

The phase difference curves measured by each receiver are shown in Figure 5.
As explained in Section 2, the presented curves are relative measurements. Hence,
at this point we cannot make conclusions from the different absolute levels of the

measurements, and instead focus on their relative shape. From the SGO curves (top panel) using existing receivers, we see that the measurement from Luleå (violet) and Kiruna (cyan) are noisier and contain probable measurement artefacts. For example, the Kiruna data close to 70° latitude shows a probable phase jump. The measurements with the new receivers shown on the bottom panel of Figure 5 are consistent when compared to each other. When comparing the two data sets, we find good overall correspondence between adjacent measurements of different receiver types.

To process with tomographic inversion, we first reduce the phase curve sampling rate by averaging. However, the high-resolution phase curves are simultaneously used to estimate the variances of the measurement error. Thus we get an error variance estimate for each measurement point of the low resolution phase curve used in the actual inversion computation. While estimating the measurement error variance, we also obtain information that can be used to handle the phase jump errors. Specifically, we set a threshold value for the variance and if it is exceeded, we assume that the signal has experienced disturbances that have caused unknown phase jumps. As mentioned at the end of Section 3, we consider the measurements after the disturbance as a new independent observation with a new unknown phase offset.

9.2. Inversion

The computational domain for the tomographic reconstruction is defined by the measurement quality and geometry. For this work, we restrict the tomographic latitude range to $40° - 78°$ latitude. The minimum elevation angle for measurements is

set to 10°. The maximum altitude is set to 1000 km to accommodate the satellite

orbit altitude. The pixel size is 0.25° in the horizontal direction and 25 km in the

vertical direction. This results in a 160×40 grid. The theory matrix connecting the

measurements to grid points is then formed by discrete linear approximation of the

line integrals of satellite signal paths.

We form the inverse prior covariance matrix $\Sigma_{\mathrm{pr}}^{-1}$ of equation (28) following the

approach introduced by *Roininen et al.* [2011, 2013]. The prior distribution is

parametrized with mean value, standard deviation and directional correlation lengths.

In the vertical direction, the mean value and the standard deviation are given here us-

ing Chapman profiles [*Brekke*, 1997]. The Chapman ionisation profile is determined

by its peak value, peak altitude and scale height.

As the prior parameters have an actual physical meaning, we first choose arbitrary

but realistic prior parameter values, and then fine-tune the parameters so that the

reconstruction starts to resemble the existing SGO receiver network reconstruction

with the same data. This is mostly to show that regardless of the differences between

the algorithms, it should be possible to produce reasonably similar reconstructions

with them, when the same data is used.

We begin with a scale height of 140 km and a peak altitude of 280 km for both the

mean and the standard deviation. The peak value for mean prior electron density is

set to $4 \cdot 10^{11} \mathrm{m}^{-3}$ and the standard deviation to $2 \cdot 10^{11} \mathrm{m}^{-3}$. The higher the standard

deviation is, the less we are forcing the reconstruction to follow the prior mean. The

correlation length is defined here as the distance where the correlation between two

points drops under $1/10^{\text{(th)}}$ of the variance. The horizontal correlation length is set to 4° and the vertical to 400 km. This gives us a rather loose prior where large variations over a given mean value are likely.

After initial results, we then change the scale height to 120 km, the peak electron density to $2 \cdot 10^{11} \text{m}^{-3}$, the peak of the standard deviation to $1 \cdot 10^{10} \text{m}^{-3}$ and the horizontal correlation length to 8°. This results in a much more restrictive prior distribution.

The SGO tomography algorithm is described by *Markkanen et al.* [1995]. It uses the statistical inversion method described in Section 4 with slightly different prior assumptions than the ones in this study.

9.3. Results

As the information provided by the measurements becomes very small when the distance between satellite and receivers increases, reconstructions in Figure 6 are carried out in a smaller grid than is used for the actual computation.

When comparing the results between the two data sets it is important to keep in mind that the receiver locations have significant differences in the longitudinal direction, as can be seen from Figure 4. However, we assume longitudinal uniformity of the ionosphere during the overflight based on separate measurements from the MIRACLE magnetometer network (not shown).

Panel a) of the Figure 6 shows the tomographic reconstruction with the new algorithm using looser prior parameter values, based on data collected with the new receivers. Panel b) plots the reconstruction with the same algorithm and parame-

ters from SGO receiver data. The reconstructions have considerable similarities, but the reconstruction from the new receiver data is generally smoother throughout the reconstructed ionosphere. With the data from SGO receivers, in the reconstruction between the latitudes of 61° and 63°, there are also some faint structures in the ray direction that are quite clearly processing artifacts.

Panel c) in Figure 6 plots the results from the new algorithm with the SGO receiver data, but now with the stronger prior assumption. Panel d) plots the reconstruction with SGO's production tomography algorithm the SGO receiver data. When comparing these panels c) and d), we see that the algorithms are consistent when correspondingly strong prior distribution is used. In general, both reconstructions suffer from wave-like structure around the receivers. This would suggest that the prior is pulling the electron density too low on areas with less information. This could probably be corrected by adjusting the prior distribution.

10. Conclusions

We have implemented a new beacon satellite receiver system for 150/400 MHz dual-band transmissions. The current software is used for routine operational measurements. Once configured and operational, the receiver software automatically downloads the satellite ephemeris files and records all satellite passes. The software then performs a phase curve analysis on these measurements with another background process.

We have also produced realistic tomographic reconstruction of the ionospheric electron density with the data provided by our newly-developed and newly-deployed receivers. We have also shown that the tomographic algorithm used in this study gives results comparable to ones produced by the existing SGO receiver system. The measured phase curves of the new receiver typically have fewer phase jumps than the SGO system, which indicates that the new receiver is more sensitive.

11. Future work

After a more rigorous validation of the system using direct electron density profiles from incoherent scatter radar observations, future work will focus on deploying more 150/400 MHz beacon satellite receivers to obtain better geographical coverage. We will also focus on improving our tomographic algorithms in such a way that they can incorporate auxiliary information about electron densities from ionosondes, incoherent scatter radars and GPS receivers. Eventually the developed algorithm will be extended to the three-dimensional case.

References

Appleton, E. V. and F. W. Chapman, (1932), *Proc. Phys. Soc.*, London, 44, 246.

Hartree, D. R., (1929), *Proc. Cambridge Phil. Soc.*, 25, 47.

Austen, J. R., S. J. Franke and C. H. Liu, (1988), Ionospheric imaging using computerized tomography, *Radio Sci. 23*(3), 299–307.

Bernhardt, P. A., Selcher, C. A., Basu, S., Bust, G. R., and Reising, S. C., (2000), Atmospheric Studies with the Tri-Band Beacon Instrument on the COSMIC constellation, *TAO 11*(1), 291–312.

Bernhardt, P. A. and C. L. Siefring, (2006), New satellite-based systems for ionospheric tomography and scintillation region imaging, *Radio Sci., 41*

Bernhardt, P. A., R. P. McCoy, K. F. Dymond, J. M. Picone, R. R. Meier, F. Kamalabadi, D. M. Cotton, S. Charkrabarti, T. A. Cook, J. S. Vickers, A. W. Stephan, L. Kersley, S. E. Pryse, I. K. Walker, C. N. Mitchell, P. R. Straus, H. Ha, C. Biswas, G. S. Bust, G. R. Kronschnabl, and T. D. Raymond, (1998), Two-dimensional mapping of the plasma density in the upper atmosphere with computerized ionospheric tomography (CIT), *Physics of Plasmas*, 5, 2010–2021.

Brekke, A., (1997), *Physics of the upper polar atmosphere*, Wiley, West Sussex, England.

Calvetti, D. and E. Somersalo, (2007), *Introduction to Bayesian Scientific Computing – Ten Lectures on Subjective Computing*, Springer, New York.

Danchik, R. J., (1998), An overview of Transit development, *Johns Hopkins APL Technical Digest*, 19(1).

Davies, K. (1965), *Ionospheric Radio Propagation*, National Bureau of Standards.

Folk, Mike, et al., (2011), An overview of the HDF5 technology suite and its applications, *Proceedings of the EDBT/ICDT 2011 Workshop on Array Databases.* ACM.

Garner, T. W., T. L. Gaussiran II, J. A. York, D. M. Munton, C. M. Slack III, and A. M. Mahrous, (2009), Ionospheric Tomography Network of Egypt: A New Receiver Network in Support of the International Heliophysical Year, *Earth, Moon, and Planets*, 104, 227–235

Izsak, I. G., (1960), Orbit Determination from Simultaneous Dopplershift Measurements, *SAO Special Report #38.*

Kaipio, J., and E. Somersalo, (2005), *Statistical and Computational Inverse Problems*, Springer, New York.

Kunitsyn, V. E., and E. D. Tereshchenko, (2003), *Ionospheric Tomography*, Springer-Verlag, Berlin, Germany.

Kunitsyn, V. E., E. S. Andreeva, E. D. Tereshchenko, B. Z. Khudukon, and T. Nygrn, (1994), Investigations of the ionosphere by satellite radiotomography, *International Journal of Imaging Systems and Technology*, 5(2), 112–127.

Lassen, H., (1927), *Elektr. Nachr. Technik.*, 4, 324.

Markkanen, M., M. S. Lehtinen, T. Nygrén, J. Pirttilä, P. Helenius, E. Vilenius, E. D. Tereshchenko and B. Z. Khudukon, (1995), Bayesian approach to satellite radiotomography with applications in the Scandinavian sector, *Ann. Geophys. 13*, 1277-1287.

Mitchell, C. N., L. Kersley, J. A. T. Heaton, and S. E. Pryse, (1997), Determination of the vertical electron-density profile in ionospheric tomography: experimental results, , *Ann. Geophys. 15*, 747–752.

Mitola, III, J., (2000), *Software radio architecture: Object oriented approaches to wireless systems engineering*, John Wiley & Sons.

Norberg, J., L. Roininen, J. Vierinen, M. S. Lehtinen, and O. Amm, (2014), Ionospheric tomography in Bayesian framework with Gaussian Markov random field priors, *Radio Sci.*, submitted.

Nygrén, T., M. Markkanen, M. S. Lehtinen, E. D. Tereshchenko and B. Z. Khudukon, O. V. Khudukon, O. V. Evstafiev, and P. Pollari, (1996), Comparison of F-region electron density observations by satellite radio tomography and incoherent scatter methods, *Ann. Geophys. 14*, 1422-1428.

Nygrén, T., M. Markkanen, M. S. Lehtinen, E. D. Tereshchenko, and B. Z. Khudukon, (1997), Stochastic inversion in ionospheric radiotomography, *Radio Sci.*, 32(6), 23592372.

Rideout, W., and Coster, A., (2006), Automated GPS processing for global total electron content data, *GPS Solutions*, 10, 219-228.

Reed, J. H., (2002), *Software Radio*, Communications Engineering and Emerging Technologies Series, Prentice-Hall.

Roininen, L., M. S. Lehtinen, S. Lasanen, M. Orispää and M. Markkanen, (2011), Correlation priors, *Inverse Probl. Imag. 5*(1), 167-184.

Roininen, L., P. Piiroinen and M. S. Lehtinen, (2013), Constructing Continuous Stationary Covariances as Limits of the Second-Order Stochastic Difference Equations, *Inverse Probl. Imag.*, *7*(2), 611-647.

Raymund, T. D., J. R. Austen, S. J. Franke, C. H. Liu, J. A. Klobuchar, and J. Stalker, (1990), Application of computerized tomography to the investigation of ionospheric structures, *Radio Sci.*, 25(5), 771789.

Rüeger, J. M, (2002), Refractive Index Formulae for Radio Waves, *In Proc. FIG XXII International Congress, Washington D.C. USA.*

Yamamoto, M., (2008), Digital beacon receiver for ionospheric TEC measurement developed with GNU Radio, *Earth Planets Space 60*, e21–e24

Phase curve errors
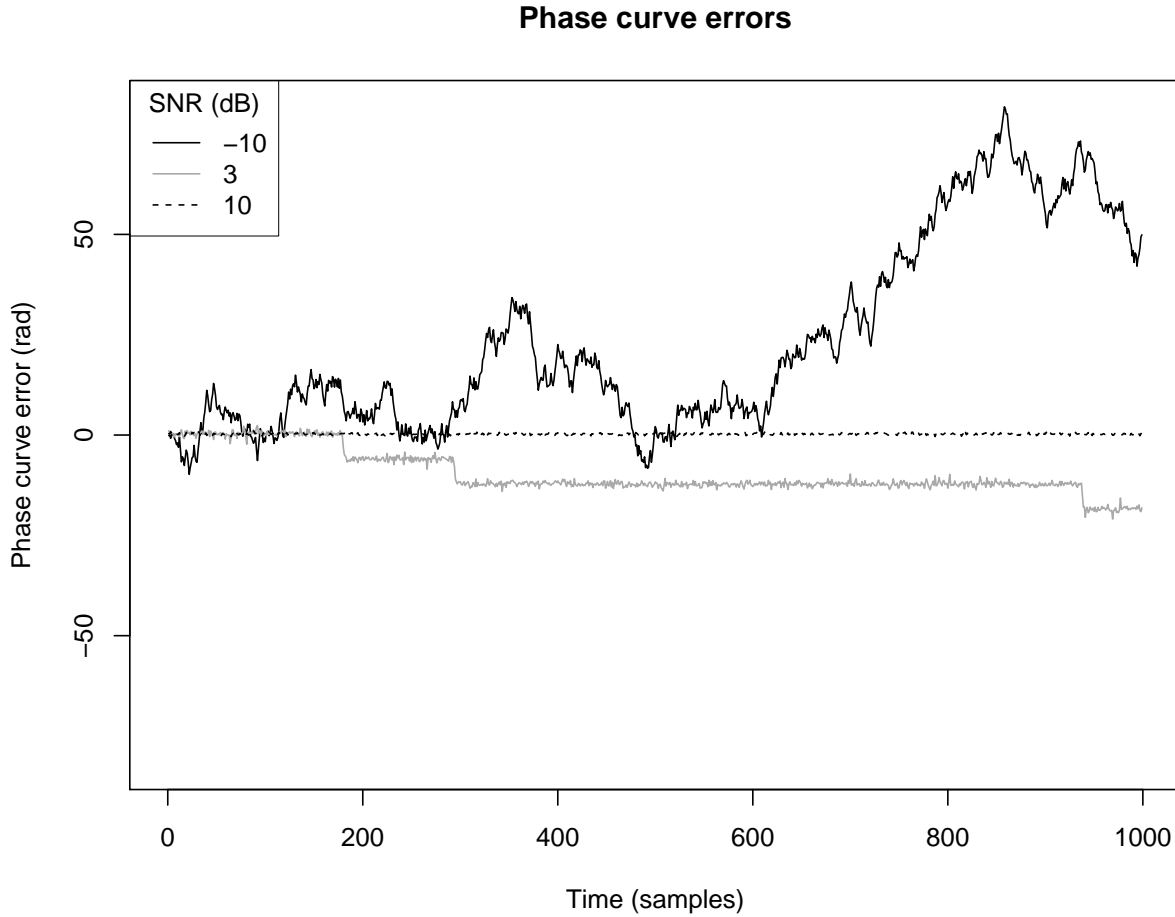
Figure 1.   Phase errors with unwanted $\pm 2\pi$ jumps. In the case of low SNR (-10 dB), the jumps are nearly random jumps uniformly between $[-\pi, \pi]$. These cannot be easily detected. In the case of medium SNR (3 dB), there are a few discrete $\pm 2\pi$ jumps. In the case of high SNR (10 dB), random jumps of $\pm 2\pi$ are extremely rare.
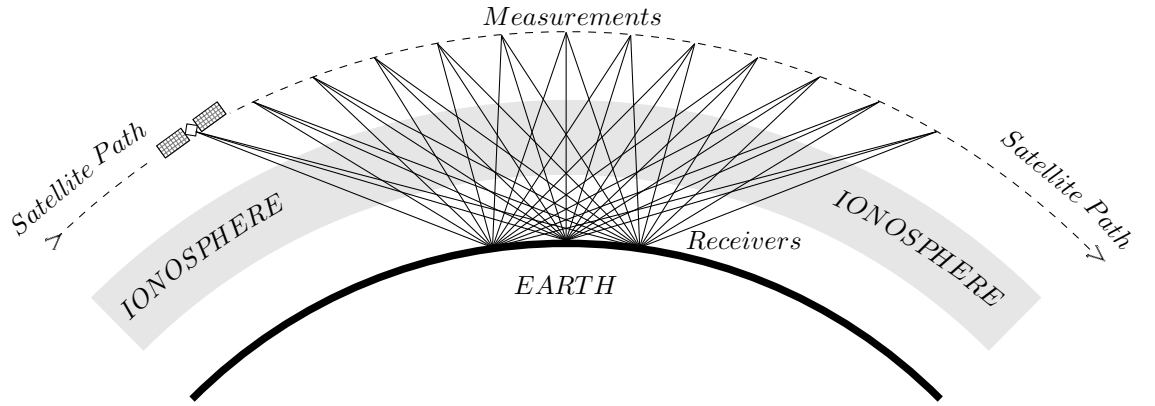
Figure 2. A conceptual diagram of an ionospheric tomography measurement. A satellite passes above ground based receivers, which measure the propagation delay for the signal transmitted by the satellite.
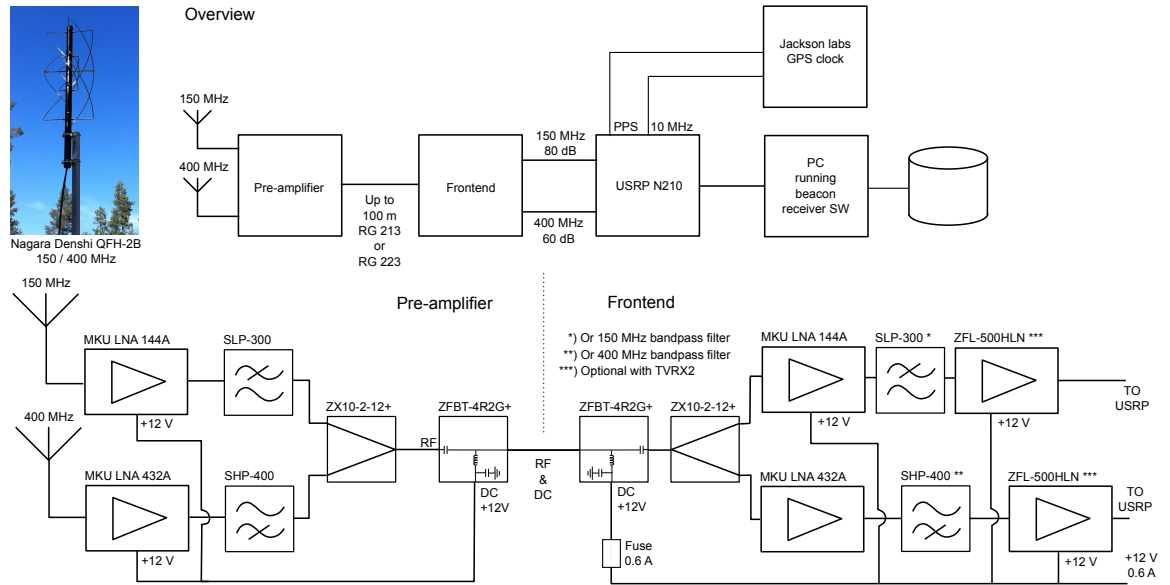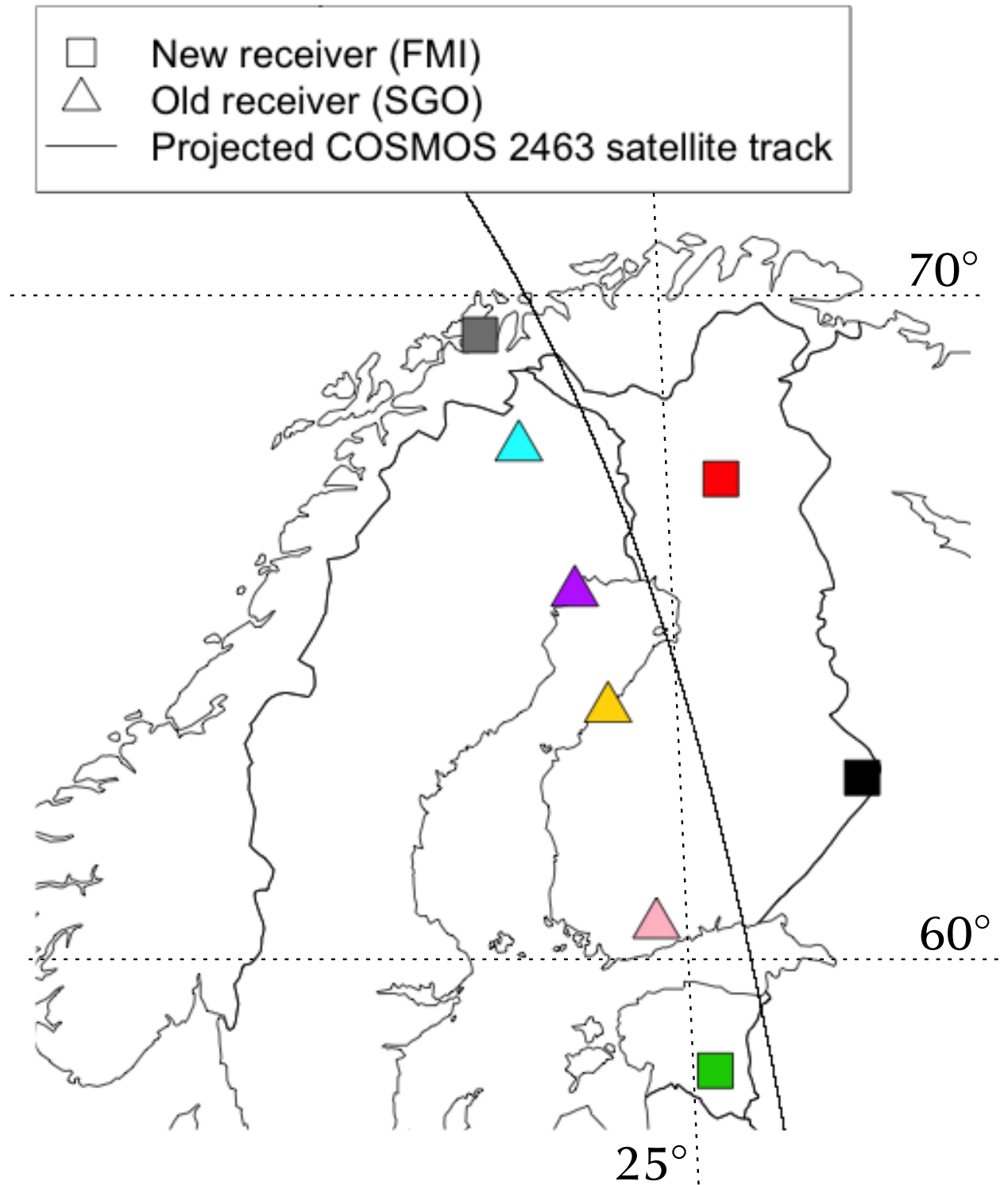

Figure 3. A block diagram of the RF front end used in the FMI beacon receiver chain.

Name	Latitude (N)	Longitude (E)
LYR	78.15	16.04
KEV	69.76	27.01
TRO	69.58	19.22
SOD	67.37	26.63
MEK	62.77	30.97
TAR	58.26	26.46

**Table 1.** Locations of new software defined ionospheric tomography receivers.

Figure 4. The new TomoScand receiver stations deployed by FMI, the old SGO receiver chain and the projected satellite path.

SGO relative phase difference curves

FMI relative phase difference curves
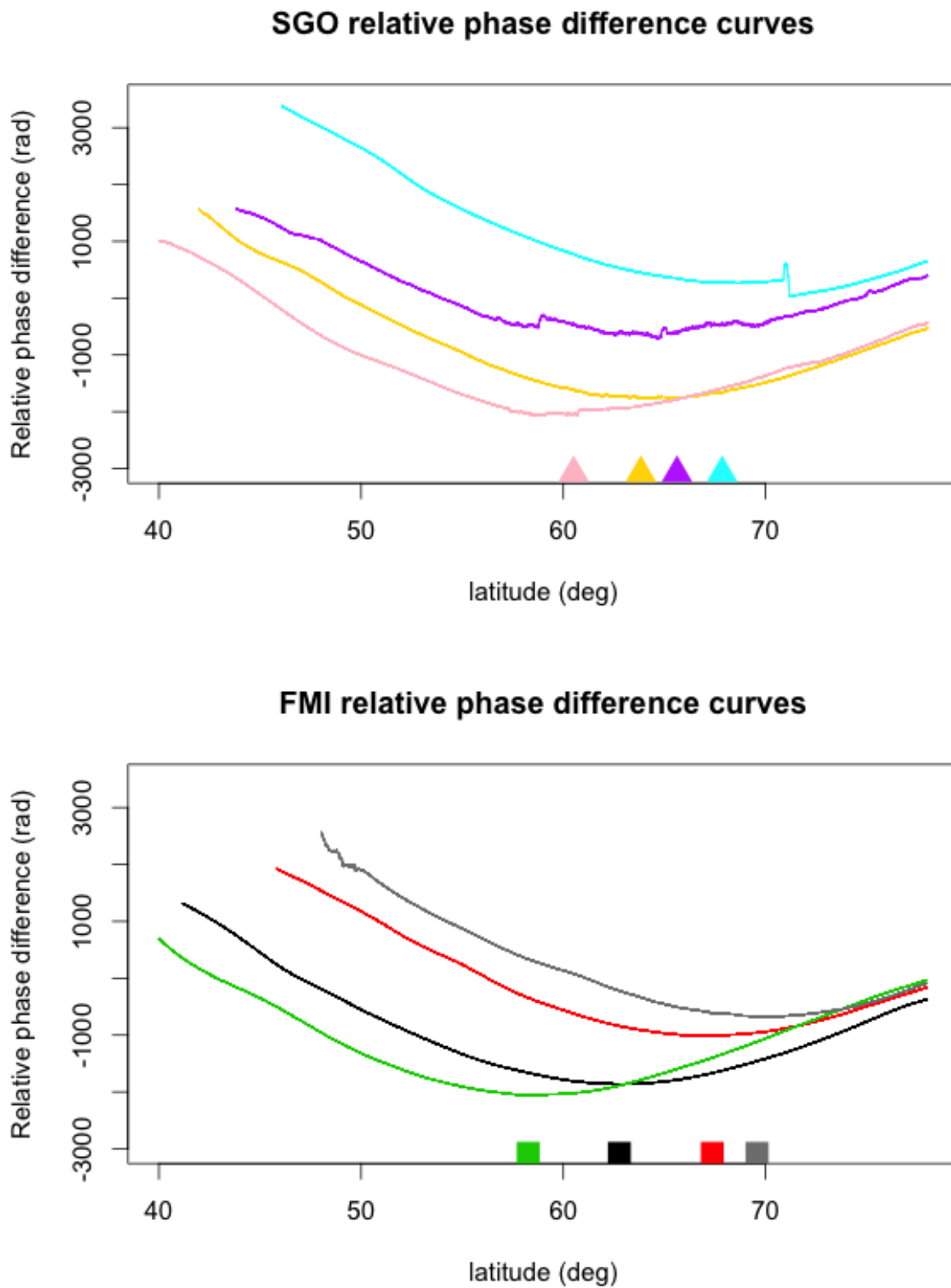
Figure 5. The relative phase difference curves from old receivers of SGO and new receivers of TomoScand/FMI receivers. Latitudes of each receiver station are marked by symbols.
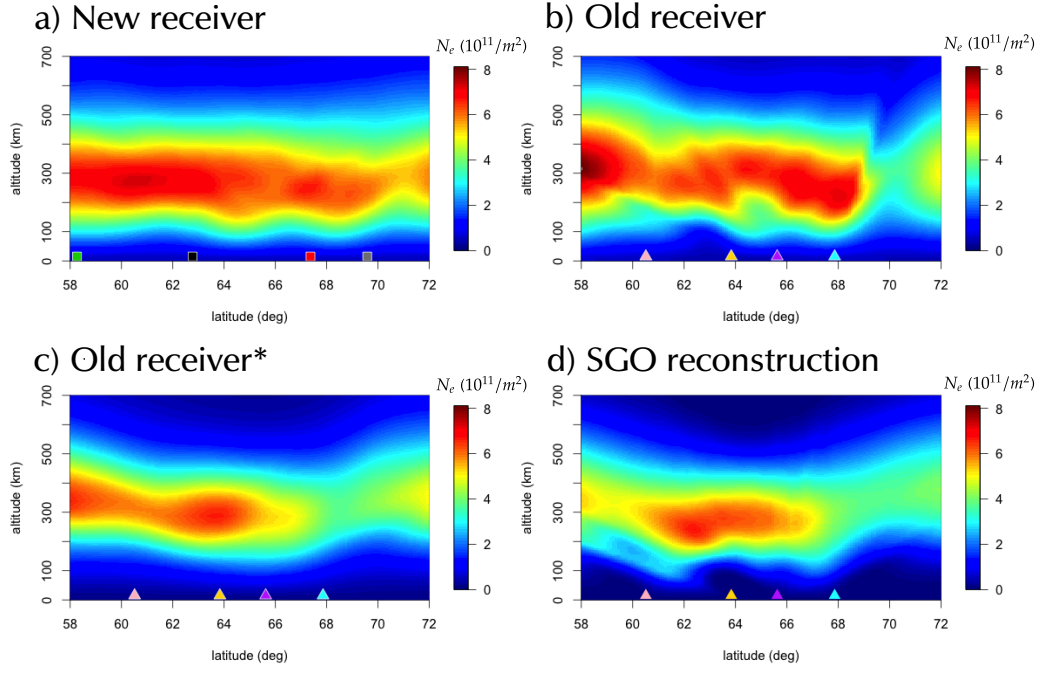
Figure 6. Tomographic reconstructions using new and old receiver data. a) A reconstruction is made with the new algorithm with the initial prior and from the new receiver data. b) The new algorithm with the initial prior and with the old receiver data. c) The new algorithm with a stronger prior (smoother) and old receiver data. d) A reconstruction with SGO's algorithm and old receiver data.